materials

MDPI

Article

Magnetic Properties of $A_2Ni_2TeO_6$ (A = K, Li): Zigzag Order in the Honeycomb Layers of Ni^{2+} Ions Induced by First and Third Nearest-Neighbor Spin Exchanges

Tatyana Vasilchikova [1], Alexander Vasiliev [1,2,3,*], Maria Evstigneeva [4], Vladimir Nalbandyan [4], Ji-Sun Lee [5], Hyun-Joo Koo [5,*] and Myung-Hwan Whangbo [5,6]

1 Department of Low Temperature Physics and Superconductivity, Lomonosov Moscow State University, Moscow 119991, Russia; t_vasilchikova@mig.phys.msu.ru
2 Quantum Functional Materials Laboratory, National University of Science and Technology "MISiS", Moscow 119049, Russia
3 Department of Theoretical Physics and Applied Mathematics, Ural Federal University, Ekaterinburg 620002, Russia
4 Faculty of Chemistry, Southern Federal University, Rostov-on-Don 344090, Russia; maevstigneeva@gmail.com (M.E.); vbn@sfedu.ru (V.N.)
5 Department of Chemistry and Research Institute for Basic Sciences, Kyung Hee University, Seoul 02447, Korea; ljisun200@khu.ac.kr (J.-S.L.); whangbo@ncsu.edu (M.-H.W.)
6 Department of Chemistry, North Carolina State University, Raleigh, NC 27695, USA
* Correspondence: vasil@mig.phys.msu.ru (A.V.); hjkoo@khu.ac.kr (H.-J.K.)

Abstract: The static and dynamic magnetic properties and the specific heat of $K_2Ni_2TeO_6$ and $Li_2Ni_2TeO_6$ were examined and it was found that they undergo a long-range ordering at T_N = 22.8 and 24.4 K, respectively, but exhibit a strong short-range order. At high temperature, the magnetic susceptibilities of $K_2Ni_2TeO_6$ and $Li_2Ni_2TeO_6$ are described by a Curie–Weiss law, with Curie-Weiss temperatures Θ of approximately −13 and −20 K, respectively, leading to the effective magnetic moment of about 4.46 ± 0.01 μ_B per formula unit, as expected for Ni^{2+} (S = 1) ions. In the paramagnetic region, the ESR spectra of $K_2Ni_2TeO_6$ and $Li_2Ni_2TeO_6$ show a single Lorentzian-shaped line characterized by the isotropic effective g-factor, g = 2.19 ± 0.01. The energy-mapping analysis shows that the honeycomb layers of $A_2Ni_2TeO_6$ (A = K, Li) and $Li_3Ni_2SbO_6$ adopt a zigzag order, in which zigzag ferromagnetic chains are antiferromagnetically coupled, because the third nearest-neighbor spin exchanges are strongly antiferromagnetic while the first nearest-neighbor spin exchanges are strongly ferromagnetic, and that adjacent zigzag-ordered honeycomb layers prefer to be ferromagnetically coupled. The short-range order of the zigzag-ordered honeycomb lattices of $K_2Ni_2TeO_6$ and $Li_2Ni_2TeO_6$ is equivalent to that of an antiferromagnetic uniform chain, and is related to the short-range order of the ferromagnetic chains along the direction perpendicular to the chains.

Keywords: metaloxides; honeycomb lattice; long-range order; short-range order; first principles calculations

Citation: Vasilchikova, T.; Vasiliev, A.; Evstigneeva, M.; Nalbandyan, V.; Lee, J.-S.; Koo, H.-J.; Whangbo, M.-H. Magnetic Properties of $A_2Ni_2TeO_6$ (A = K, Li): Zigzag Order in the Honeycomb Layers of Ni^{2+} Ions Induced by First and Third Nearest-Neighbor Spin Exchanges. *Materials* **2022**, *15*, 2563. https://doi.org/10.3390/ma15072563

Academic Editor: Alexander A. Lebedev

Received: 28 February 2022
Accepted: 24 March 2022
Published: 31 March 2022

1. Introduction

Compounds with honeycomb layers of magnetic ions attracted much attention in the field of low-dimensional magnetism [1], owing in part to Kitaev's conjecture [2] that they can have gapped and gapless liquid-like ground states in a certain range of spin exchange parameters. It has been elusive to find honeycomb-layered (Figure 1a) magnetic systems confirming Kitaev's conjecture because of the inevitable interlayer interactions, which can lead to a three-dimensional (3D) long-range ordering. In real honeycomb-layered materials, anisotropic in-plane Kitaev interactions compete with isotropic Heisenberg interactions. The ordering of magnetic moments in honeycomb layers can be zigzag (Figure 1b) or

stripy (Figure 1c) [3]. Kitaev's conjecture was originally analyzed for the spin $S = 1/2$ case, but it has subsequently been extended to $S > 1/2$ systems (in particular, $S = 1$), although these systems are not exactly solvable [4]. It was shown that the bond-dependent Kitaev interaction model can be realized in two-dimensional (2D) Mott insulators if there exists strong Hund coupling of electrons at the cation sites and strong spin-orbit coupling at the anion sites [4]. The iridate Na_2IrO_3 with honeycomb layers of low-spin Ir^{4+} (d^5, $S = 1/2$) ions [5–7] and the ruthenium chloride α-$RuCl_3$ with honeycomb layers of low-spin Ru^{3+} (d^5, $S = 1/2$) ions [8–10] were examined as the $S = 1/2$ systems that can capture the basics of Kitaev magnetism. The iridate β-Li_2IrO_3 has also been examined for Kitaev magnetism, but its Ir^{4+} ions form a 3D framework rather than honeycomb layers [11,12]. The magnetic structure in the honeycomb layers of Na_2IrO_3 is consistent with a zigzag order (i.e., FM zigzag chains of Ir^{4+} ions are antiferromagnetically coupled, Figure 1b) or a stripy order (i.e., AFM zigzag chains of Ir^{4+} ions are ferromagnetically coupled, Figure 1c) [6]. The magnetic structure of α-$RuCl_3$ is more consistent with a zigzag order than with a stripy order [9]. The layered-phase $A_3Ni_2SbO_6$ (A = Li, Na) [13,14] consists of honeycomb layers of $S = 1$ ions (i.e., Ni^{2+} ions). Each honeycomb layer consists of edge-sharing NiO_6 octahedra each containing a Ni^{2+} ion, in which every hexagon of Ni^{2+} ions has its center occupied by a Sb^{5+} cation to form a SbO_6 octahedron (Figure 1d). The magnetic structure of $A_3Ni_2SbO_6$ (A = Li, Na) in the honeycomb layers of Ni^{2+} ions is described by a zigzag order [13], similar to the one found for the $S = 1/2$ systems Na_2IrO_3 and α-$RuCl_3$.

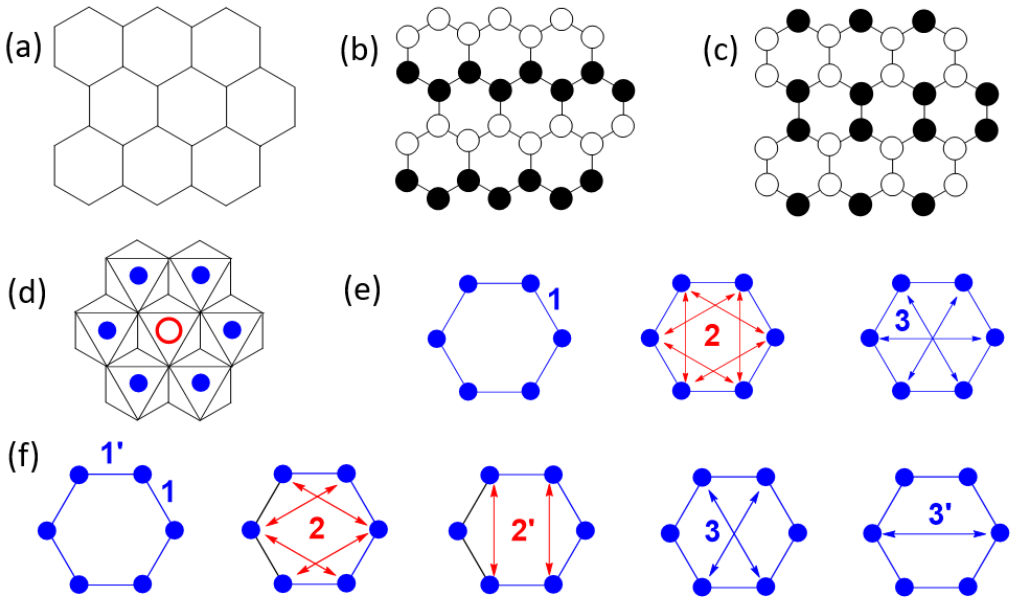

Figure 1. (**a**) A simplified view of a honeycomb layer made up of magnetic ions. (**b**) A zigzag order of magnetic moments in a honeycomb layer. (**c**) A stripy order of magnetic moments in a honeycomb layer. (**d**) A honeycomb layer of magnetic ions (solid blue circles) in which the center of every hexagon of magnetic ions is occupied by a cation (e.g., Na^+ in Na_2IrO_3, Sb^{5+} in $A_3Ni_2SbO_6$, Te^{6+} in $A_2Ni_2TeO_6$, $(P\text{-}P)^{8+}$ dimer in $NiPS_3$). (**e**) First NN spin exchange (J_1), second NN spin exchange (J_2), and third NN spin exchange (J_3) in a honeycomb layer made up of regular hexagons of magnetic ions. (**f**) First NN spin exchange (J_1 and J_1'), second NN spin exchange (J_2 and J_2'), and third NN spin exchange (J_3 and J_3') in a honeycomb layer made up of slightly distorted hexagons of magnetic ions (e.g., 2-fold rotational symmetry).

So far, it is not clear why the honeycomb layers of these magnetic systems form a zigzag order, namely, why they adopt FM zigzag chains that are antiferromagnetically coupled. To understand the cause for this ordering, it is necessary to know the spin exchanges between the first, second, and third nearest-neighbor (NN) magnetic ions, which are J_1, J_2, and J_3 depicted in Figure 1e, respectively, when a honeycomb layer is made up of

regular hexagons of magnetic ions. However, when these hexagons are lower in symmetry (e.g., 2-fold rotational symmetry), the first, second, and third NN spin exchanges are each split into two different ones, as depicted in Figure 1f. Zvereva et al. evaluated three spin exchanges of $A_3Ni_2SbO_6$ (A = Li, Na) [13] (namely, the first NN exchanges J_1 and J_1' as well as the third NN exchanges J_3 and J_3', Figure 1f), and found that J_1 is AFM, J_1' is FM, while the third NN spin exchanges J_3 and J_3' are practically zero. Although this is consistent with a zigzag order in $A_3Ni_2SbO_6$ (A = Li, Na), we note that a zigzag order also occurs in the honeycomb layers of M^{2+} (M = Fe, Co, Ni) ions in the sulfides MPS_3, in which each hexagon of M^{2+} ions has its center occupied by a $P_2S_6^{4-}$ ion (Figure 1d) to form MS_6 octahedra. The strongest spin exchange of $NiPS_3$ was found to be the third NN exchanges (J_3 and J_3'), which are strongly AFM, while the first NN spin exchanges (J_1 and J_1') are FM and are weaker than the third NN exchanges by a factor greater than three [15]. Thus, the zigzag order of $NiPS_3$ is caused by the strongly AFM third NN spin exchanges. This finding makes it necessary to check if the third NN spin exchanges vanish in $A_3Ni_2SbO_6$ (A = Li, Na) as reported [13].

Honeycomb layers of Ni^{2+} ions similar to those of $A_3Ni_2SbO_6$ (A = Li, Na) are also present in $A_2Ni_2TeO_6$ (A = K, Li) [16–19]. Formally, $A_2Ni_2TeO_6$ results from $A_3Ni_2SbO_6$ by replacing the Sb^{5+} ion with a Te^{6+} ion, by removing one cation A^+ to satisfy the charge balance requirement, and by changing the layer stacking mode leading to trigonal prismatic and tetrahedral coordination for K^+ and Li^+, respectively. In the present work, we probed the static and dynamic magnetic properties of $A_2Ni_2TeO_6$ (A = K, Li) and found that they are very similar to those of $A_3Ni_2SbO_6$ (A = Li, Na), and we determined the spin exchanges (Figure 1f) of $A_2Ni_2TeO_6$ using the energy-mapping analysis [20,21] to show that the honeycomb layers of not only $A_2Ni_2TeO_6$ but also $A_3Ni_2SbO_6$ have a zigzag magnetic order for the same reason as found for $NiPS_3$. Thus, the cause for the zigzag order of not only $A_2Ni_2TeO_6$ (A = K, Li) but also $A_3Ni_2SbO_6$ (A = Li, Na) is the third NN spin exchange, which is strongly AFM, as found for NPS_3.

Both static and dynamic magnetic properties of $A_2Ni_2TeO_6$ (A = K, Li) evidence the behavior inherent in a magnet with reduced dimensionality, and the long-range order in these compounds is preceded by a short-range order. These observations are fully supported by specific heat measurements, which reveal sharp λ-type singularities establishing the occurrence of a Néel order. We show that the honeycomb layers of $A_2Ni_2TeO_6$ (A = K, Li) and $Li_3Ni_2SbO_6$ adopt a zigzag order, in which zigzag ferromagnetic chains are antiferromagnetically coupled, and that the short-range order of $Li_2Ni_2TeO_6$ and $K_2Ni_2TeO_6$ arises from the short-range order of the ferromagnetic chains along the direction perpendicular to the chains.

2. Sample Preparation and X-ray Diffraction

2.1. $K_2Ni_2TeO_6$

Light-green samples of $K_2Ni_2TeO_6$ were prepared by conventional solid-state synthesis. Since the material is highly hygroscopic, it was necessary to protect it from the atmospheric moisture (see the Supplementary Materials for details). In agreement with the previous data [18], the XRD pattern (Supplementary Figure S1) shows that our sample of $K_2Ni_2TeO_6$ represents a hexagonal superlattice of the P2 type, space group $P6_3/mcm$, with only weak extra reflections. Least squares refinements resulted in the lattice parameters a = 5.258(3), c = 12.417(1) Å, and c/a = 2.362, which are consistent with the literature data [18]. The small differences in the absolute values are systematic and may hence be due to uncertainties in our refined sample displacement and/or in the wavelengths used. Thus, it is important to compare the axial ratios. Masese et al. [18] reported a slightly higher c/a ratio of 2.370, together with the dark green color of their sample, which suggests the presence of some Ni^{3+} ions, presumably due to potassium deficiency. Chemical analysis of our light-green sample by reverse redox titration [22] yielded the oxidation state of 2.01 ± 0.01 for Ni, thus confirming the stoichiometry. In contrast, our potassium-deficient samples were black, containing a considerable amount of Ni^{3+} ions and exhibiting much

larger *c/a* ratios. This is a common feature of the present class of structures: the oxidation of an octahedral cation results in the *a*-axis contraction, and the loss of the interlayer alkali ions, in the *c*-axis expansion. However, the deviation from stoichiometry in the reported structure [18] is evidently small and the reported structure is quite reasonable, so we did not attempt a re-refinement.

2.2. $Li_2Ni_2TeO_6$

We prepared $Li_2Ni_2TeO_6$ from $Na_2Ni_2TeO_6$ by an ion-exchange reaction [16] (see the Supplementary Materials for details). Previously, the XRD powder pattern (Supplementary Figure S2) was indexed in the space group *Cmca* by analogy with T2-$Li_2NiMn_2O_6$ [23]. The same preparation route and the same space group were adopted by Grundish et al. [17], and the orthorhombic lattice parameters are in reasonable agreement (Table 1). $Li_2Ni_2TeO_6$ is not isostructural with its sodium precursor (*P6$_3$/mcm*) because small Li^+ ions cannot be accommodated in the trigonal prismatic sites (i.e., Na^+ ion sites), so the adjacent honeycomb $(Ni_2TeO_6)^{2-}$ layers are shifted to provide tetrahedral interlayer sites suitable for Li^+ ions, as found in T2-$Li_2NiMn_2O_6$ [23]. Unfortunately, crystal structure refinement of the T2-type $Li_2Ni_2TeO_6$ [17] resulted in unrealistic bond lengths and bond valence sums (BVSs) (Table 2), and our refinement results were not better. The reasons for this might be: (i) Admixture of foreign phase(s): the zoomed-in view of the XRD pattern (Figure 5 in [17]) reveals a strong unindexed reflection at $2\Theta \approx 17.53^\circ$. Visually, it might seem to be the $\alpha 2$ component of the strongest reflection ($2\Theta \approx 17.38^\circ$), but their separation is three times larger than the doublet separation. Much weaker shoulders are seen in our patterns as well (Figure S2). (ii) The powder patterns are diffuse in nature arising from the stacking faults due to the layer gliding, which is induced by the ion-exchange transforming the space group of the crystal structure from *P6$_3$/mcm* to *Cmca*. (iii) X-ray diffraction measurements have a low sensitivity to the positions of light atoms (Li and O) in the presence of heavy elements (Te and Ni). Thus, in the X-ray crystal structure reported for $Li_2Ni_2TeO_6$ [17], some Li, O1, and O2 positions are known only in three decimal places. Thus, it is important to have more accurate atomic positions. The crystal structure of $Li_2Ni_2TeO_6$ was optimized by DFT calculations [17], but the resulting atomic positions were not reported. Thus, we optimized the crystal structure of $Li_2Ni_2TeO_6$ by DFT + U calculations with U_{eff} = 4 eV, and the optimized atomic positions are summarized in Supplementary Table S1.

Table 1. Lattice parameters of $Li_2Ni_2TeO_6$ (*Cmca*) from different sources.

Source	a, Å	b, Å	c, Å	V, Å^3
[16]	8.9667 (18)	5.1574 (14)	10.1878 (26)	471.1
[17]	8.9925 (4)	5.1469 (2)	10.1691 (5)	470.7
This work	8.9945 (19)	5.1488 (12)	10.1628 (18)	470.6

The average Li-O, Ni-O, and Te-O bond lengths of $Li_2Ni_2TeO_6$, determined from the X-ray diffraction and our DFT + U optimized structures, are compared in Table 2, and so are the oxidations states for the Li, Ni, Te, and O atoms of $Li_2Ni_2TeO_6$ obtained from bond valence sum (BVS) calculations based on the two crystal structures. According to the optimized crystal structure, the oxidation states of Li and Ni are very close to those expected from the ionic electron counting scheme (+1 and +2, respectively). In contrast, the oxidation state of Te is considerably smaller than expected from the ionic electron counting scheme (i.e., +5.29 vs. +6), while that of O is considerably higher than expected (i.e., −1.72/−1.87 vs. −2).

Table 2. Average lengths of the Li-O, Ni-O, and Te-O bonds and oxidation states of Li, Ni, Te, and O of $Li_2Ni_2TeO_6$ expected.

(a) Average bond lengths			
Bonds	Sum of Ionic Radii [24]	X-ray Diffraction [17]	Optimized (This Work)
Li-O	1.98	2.20	2.08
Ni-O	2.07	2.13	2.07
Te-O	1.94	1.87	1.97
(b) Oxidation states from bond valence sum analysis [25]			
	Expected [a]	X-ray Diffraction [17]	Optimized (This Work)
Li	+1	+0.68	+0.82
Ni	+2	+2.13	+1.99
Te	+6	+6.98	+5.29
O1 (16g)	−2	−2.15	−1.87
O2 (8f)	−2	−1.70	−1.72

[a] From the ionic electron counting scheme.

3. Results and Discussion

3.1. Magnetic Properties

3.1.1. Magnetic Susceptibility and Magnetization

The magnetic susceptibilities, χ(T), of $Li_2Ni_2TeO_6$ and $K_2Ni_2TeO_6$ were measured at B = 0.1 T in the temperature range of 2–300 K using a Quantum Design PPMS-9T system, and their isothermal magnetizations, $M(B)$, using a Quantum Design MPMS-7T SQUID-VSM magnetometer under an external field up to 7 T at various temperatures after cooling the sample at zero magnetic field. Results of zero-field-cooled (ZFC) and field-cooled (FC) measurements carried out for $Li_2Ni_2TeO_6$ and $K_2Ni_2TeO_6$ as well as magnetization curves are shown in Figure 2a–c. A small divergence between the results of ZFC and FC measurements indicates the presence of a modest spin disorder, due most likely to impurity-related effects. On lowering the temperature, the magnetic susceptibilities of both $Li_2Ni_2TeO_6$ and $K_2Ni_2TeO_6$ exhibit a broad maximum, χ_{max}, at $T_{max} \approx 34$ K, then the value drops by about one third of χ_{max}. The values of the Néel temperatures, T_N, deduced as the temperature, T, at which the derivative $d\chi(T)/dT$ shows a maximum (not shown), are ~22.8 K for $K_2Ni_2TeO_6$ and ~24.4 K for $Li_2Ni_2TeO_6$. These T_N values are considerably lower than T_{max}, signaling the presence of strong short-range correlations. We note that AFM uniform chains exhibit a broad magnetic susceptibility maximum due to their short-range magnetic order. The occurrence of a magnetic susceptibility maximum in $A_2Ni_2TeO_6$ (A = Li, K) and $A_3Ni_2SbO_6$ (A = Li, Na) [13,14] suggests that their magnetic properties possess a one-dimensional (1D) character, although their honeycomb magnetic lattices are 2D in nature.

The high-temperature magnetic susceptibility can be fitted by the Curie–Weiss law plus a temperature-independent term, χ_0:

$$\chi = \chi_0 + \frac{C}{T - \Theta} \quad (1)$$

where Θ is the Weiss temperature, and C is the Curie constant, $C = N_A \mu_{eff}{}^2 \mu_B{}^2 / 3k_B$ (μ_{eff} is the effective magnetic moment, while N_A, μ_B, and k_B are Avogadro's number, Bohr magneton, and Boltzmann constant, respectively). The diamagnetic contributions of $K_2Ni_2TeO_6$ and $Li_2Ni_2TeO_6$ were estimated to be $\chi_0 = -1.38\ 10^{-4}$ and $-1.1\ 10^{-4}$ emu/mol, respectively, by summing the Pascal's constants [26]. The χ_0 values were fixed to reduce the number of variable parameters during the fitting analysis. From this analysis, it was found that $\Theta = -13$ K for $K_2Ni_2TeO_6$ and -20 K for $Li_2Ni_2TeO_6$, implying the presence of dominant

antiferromagnetic interactions while, per formula unit (f.u.), μ_{eff} = 4.45 μ_B for $K_2Ni_2TeO_6$ and 4.47μ_B for $Li_2Ni_2TeO_6$. The effective g-factor obtained from ESR data (see below) is about $g \approx 2.2$. The result hence well agrees with the theoretical estimate of the effective magnetic moment equal to 4.4 μ_B/f.u. for both compounds, where n is the number of Ni^{2+} ions per formula unit, assuming Ni^{2+} in a high-spin configuration (S = 1).

$$\mu_{theor} = \sqrt{g^2 n S(S+1)\mu_B^2} \quad (2)$$

The magnetic susceptibility of $A_2Ni_2TeO_6$ (A = K, Li) can be analyzed on the basis of the high-temperature series expansion (HTSE) approach for a 2D planar honeycomb lattice using the Rushbrook and Wood model [27]. Then, the $\chi(T)$ curve in the paramagnetic region can be described by:

$$\chi = \frac{2Ng^2\beta^2}{3kT} \cdot \frac{1}{1 + Ax + Bx^2 + Cx^3 + Dx^4 + Ex^5 + Fx^6} \quad (3)$$

where $x = |J|/kT$, A = 4, B = 7.333, C = 7.111, D = –5.703, E = –22.281, and F = 51.737.[27] Fitting the $\chi(T)$ curve by Equation (3) in the range of 50–300 K yields $J = -8 \pm 1$ K for both compounds. The magnetization isotherms, $M(B)$, taken at 2 K (Figure 2c) demonstrate upward deviations from the linear dependences, suggesting spin–flop transitions at $B_{SF} \approx 4.7$ T and 4.4 T for $Li_2Ni_2TeO_6$ and $K_2Ni_2TeO_6$, respectively. Table 3 summarizes the parameters describing the magnetic subsystems of $A_2Ni_2TeO_6$ (A = Li, K), obtained from the magnetic susceptibility and magnetization measurements.

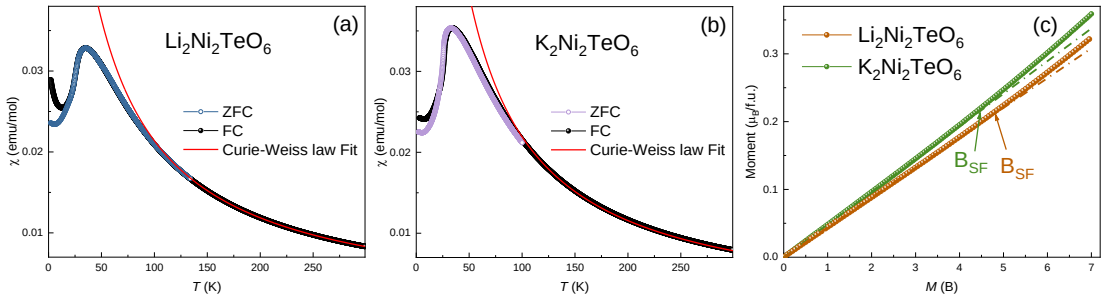

Figure 2. ZFC and FC magnetic susceptibilities of (**a**) $Li_2Ni_2TeO_6$ and (**b**) $K_2Ni_2TeO_6$ taken at B = 0.1 T. The solid lines are the fits by the Curie–Weiss law, dashed green lines—Rushbrook–Wood model fit. (**c**) Magnetizations of $Li_2Ni_2TeO_6$ and $K_2Ni_2TeO_6$ at T = 2 K. The fields of the spin–flop transition, B_{sf}, are marked by arrows.

Table 3. Parameters describing the magnetic subsystems of $A_2Ni_2TeO_6$ (A = K, Li) tellurates.

	Θ, K	**μ_{eff}, μ_B/f.u.**	**T_{max}, K**	**T_N, K**	**J, K**	**B_{SF}, T**
$Li_2Ni_2TeO_6$	-20 ± 1	4.47 ± 0.01	~34	24.4 ± 0.2	-8 ± 1	~4.7
$K_2Ni_2TeO_6$	-13 ± 1	4.45 ± 0.01	~34	22.8 ± 0.2	-8 ± 1	~4.4

3.1.2. Electron Spin Resonance

Electron spin resonance (ESR) studies were carried out using an X-band ESR spectrometer CMS 8400 (ADANI) ($f \approx 9.4$ GHz, $B \leq 0.7$ T), equipped with a low-temperature mount, operating in the range of T = 6–300 K. The effective g-factors were calculated using an external reference for the resonance field, i.e., BDPA (*a*,*g*-bisdiphenylene-*b*-phenylallyl), for which g_{et} = 2.00359. The ESR data in the paramagnetic phase ($T > T_N$) show a single broad Lorentzian line-shape ascribable to Ni^{2+} ions in octahedral coordination [28] for both $K_2Ni_2TeO_6$ and $Li_2Ni_2TeO_6$ (Supplementary Figure S10). The main ESR parameters

(effective g-factor, the ESR linewidth, and the integral ESR intensity) were deduced by fitting the experimental spectra with the Lorentzian profile [29]:

$$\frac{dP}{dB} \propto \frac{d}{dB}\left[\frac{\Delta B}{\Delta B^2 + (B - B_r)^2} + \frac{\Delta B}{\Delta B^2 + (B + B_r)_2}\right] \quad (4)$$

where P is the power absorbed in the ESR experiment, B_r is the resonance field, and ΔB is the linewidth. The integral ESR intensity, χ_{ESR}, which is proportional to the number of magnetic spins, was estimated by double integration of the first derivative ESR spectrum, dP/dB. Evidently, the temperature dependence of $\chi_{ESR}(T)$ follows the Curie–Weiss relationship and agrees well with the static magnetic susceptibility $\chi(T)$, as shown in the upper panels of Figure 3.

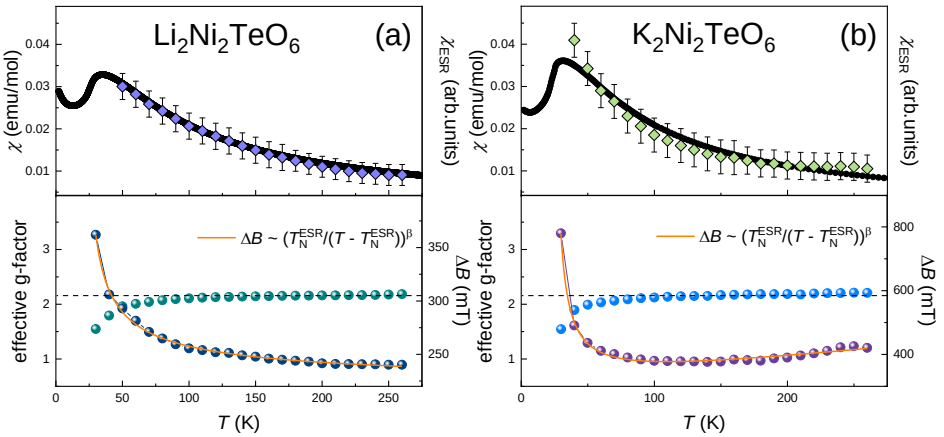

Figure 3. The temperature dependence of the main ESR parameters of (**a**) $K_2Ni_2TeO_6$ and (**b**) $Li_2Ni_2TeO_6$ derived from fitting the absorption line with the Lorentzian profile: the integral ESR intensity is shown in the upper panel, and the effective g-factor and the ESR linewidth, ΔB, in the lower panel. The orange solid curves represent an approximation in accordance with a modified Huber theory (Equation (5)), as described in the text for (**a**), and in the framework of Kawasaki–Mori–Huber theory (Equation (6)) for (**b**).

The average effective g-factor of 2.20 ± 0.03 remains almost temperature-independent in the paramagnetic phase down to ~100 K (lower panels of Figure 3), and then the visible shift of the resonant field to higher magnetic fields begins upon approaching the Néel temperature from above. This behavior implies the presence of strong short-range correlations at temperatures noticeably higher than T_N, which is characteristic of the systems with spin frustration and low dimensionality [29].

The linewidth, ΔB, of $K_2Ni_2TeO_6$ shows three different dynamic regimes: It decreases weakly and almost linearly on lowering the temperature down to ~150 K, then remains constant down to ~100 K. Upon a further decrease in the temperature, the absorption line broadens significantly and the ESR signal vanishes in the vicinity of the Néel temperature, indicating the opening of an energy gap for resonance excitations, e.g., due to the occurrence of a long-range order. Similar spin dynamics were observed recently for $A_3Ni_2SbO_6$ (A = Li, Na) with a honeycomb lattice of Ni^{2+} ions [13]. Following the same procedure, we treated $\Delta B(T)$ in the frame of the critical broadening model using the modified Huber's formula [30–33] with the third linear term to account for the $\Delta B(T)$ behavior over the whole temperature range:

$$\Delta B(T) = \Delta B^* + A\left[\frac{T_N^{ESR}}{T - T_N^{ESR}}\right]^{\beta} + DT \quad (5)$$

where the first term ΔB^* describes the exchange narrowed linewidth, which is temperature-independent. The second term describes the critical behavior, with $T_N{}^{ESR}$ as the temperature of the order–disorder transition and β as the critical exponent. The third term relates to

the temperature-linear spin-lattice relaxation term. The solid line on the lower panel of Figure 3a represents a least-squares-fitting of $\Delta B(T)$. The best fitting was obtained with $\Delta B^* = 290 \pm 5$ mT, $\beta \approx 1 \pm 0.05$, and $D = 0.4$ mT/K. Clearly, T_N^{ESR} is in good agreement with T_N. According to Kawasaki's approach [25,26], the absolute value of the critical exponent can be expressed as $\beta = [(7 + \eta)\nu/2 - 2(1 - \zeta)]$, where ν describes the divergence of the spin-correlation length, η is a critical exponent for the divergence of static correlations, and ζ reflects the divergence of the specific heat. Using the values $\eta = \zeta = 0$ and $\nu = 2/3$ for 3D antiferromagnets in the Heisenberg model, β becomes 1/3. Thus, the value of $\beta \approx 1$ extracted for $K_2Ni_2TeO_6$ is noticeably higher than 1/3 but is still below the value expected for pure 2D antiferromagnets (i.e., $\beta \approx 3/2$) [34,35], but it is quite comparable to the β reported for other related quasi-2D Ni^{2+} compounds $A_3Ni_2SbO_6$ (A = Li, Na) [13] and Li_4NiTeO_6 [36]. According to Kawasaki–Mori–Huber theory, the temperature variation of ΔB of $Li_2Ni_2TeO_6$ can be described as:

$$\Delta B(T) = \Delta B^* + A\left[\frac{T_N^{ESR}}{T - T_N^{ESR}}\right]^{\beta} \quad (6)$$

The best agreement by the least square method was obtained with the following parameters: $\Delta B^* = 217 \pm 5$ mT and $\beta = 0.60 \pm 0.05$. Thus, the analysis of spin dynamics supports the picture of rather a 2D character of magnetic correlations for both $K_2Ni_2TeO_6$ and $Li_2Ni_2TeO_6$. Spin-dynamic parameters of the studied compounds are summarized in Table 4.

Table 4. The spin-dynamic parameters in $A_2Ni_2TeO_6$ (A = K and Li) tellurates.

	Effective *g*-Factor	**ΔB^*, mT**	***D*, mT/K**	**β**
$Li_2Ni_2TeO_6$	2.20 ± 0.03	217 ± 5	-	0.60 ± 0.05
$K_2Ni_2TeO_6$	2.20 ± 0.03	290 ± 5	0.4	1 ± 0.05

3.1.3. Specific Heat

The specific heat, $C_p(T)$, of $A_2Ni_2TeO_6$ (A = Li, K) has been measured using a relaxation method of a Quantum Design PPMS-9T. The data were collected at the zero magnetic field as well as under applied fields of 3, 6, and 9 T in the temperature range of 2–70 K. The $C_p(T)$ vs. T plots for $K_2Ni_2TeO_6$ and $Li_2Ni_2TeO_6$ are shown in Figure 4a,b. A λ-type peak is observed at T_N for both $K_2Ni_2TeO_6$ and $A_2Ni_2TeO_6$, which clearly shows an occurrence of long-range antiferromagnetic order. These ordering temperatures, T_N, coincide with the temperatures at which the peaks of the $d(\chi T)/dT$ vs. T plot occur (i.e., the Fisher specific heat) [37,38], which is characteristic of low-dimensional antiferromagnets with strong short-range correlations. The positions of T_N slightly shift toward the lower temperatures in the applied external magnetic field, as shown in the lower insets in Figure 4a,b, which is typical for antiferromagnetic compounds. To examine the magnetic contribution to specific heat in the title compounds, the $C_p(T)$ curve has been measured for the isostructural non-magnetic system $Na_2Zn_2TeO_6$. Application of the scaling procedure [39] allows extracting magnetic specific heat, $C_m(T)$, as shown in the upper insets in Figure 4a,b. According to these data, the magnetic entropy, S_m, released below T_N is 6.74 and 5.71 J/mol·K for Li- and K-compounds, respectively. These values are to be compared with the thermodynamic limit $S_m = nR\ln(2S + 1) = 18.27$ J/mol·K at $n = 2$ and $S = 1$, meaning that the dominant part of the magnetic entropy is released above T_N.

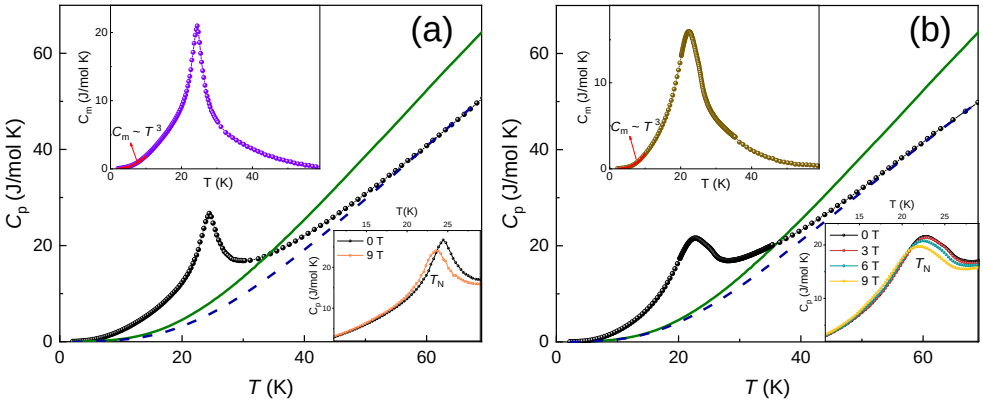

Figure 4. Temperature dependences of the specific heat in $Li_2Ni_2TeO_6$ (**a**) and $K_2Ni_2TeO_6$ (**b**). The data for $Na_2Zn_2TeO_6$ are shown by solid lines. The dashed lines represent the reference curves obtained through the scaling procedure [39]. Lower insets represent $C_p(T)$ curves measured at various magnetic fields. Upper insets represent temperature dependences of magnetic specific heat, C_m.

3.2. Spin Exchanges Leading to a Zigzag Magnetic Order

3.2.1. Computational Details

To extract the values of the spin exchanges in $A_2Ni_2TeO_6$ (A = K, Li) and $Li_3Ni_2SbO_6$ (A = Li, Na), we carried out spin-polarized DFT calculations by using the frozen-core projector augmented plane wave met [40,41], encoded in the Vienna ab initio simulation package [42], and the PBE exchange-correlation functionals [43]. The electron correlation associated with the 3*d* states of Ni was taken into consideration by performing the DFT + U calculations [44] with the effective on-site repulsion $U^{eff} = U - J$ on magnetic ions. All our DFT calculations used the plane wave cutoff energy of 450 eV and the threshold of 10^{-6} eV for self-consistent-field energy convergence. To relax the atom positions, DFT + U calculations (with U_{eff} = 4 eV) were performed using a set of (4 × 6 × 4) k-points with the criterion of 5×10^{-4} eV/Å for the relaxation of the atom positions. Our DFT + U calculations employed a set of (4 × 4 × 4) k-points for $Li_2Ni_2TeO_6$, (5 × 5 × 3) k-points for $K_2Ni_2TeO_6$, and (4 × 2 × 4) k-points for $Li_3Ni_2SbO_{12}$. As a representative example for the $A_3Ni_2SbO_6$ (A = Li, Na) family, we examined $Li_3Ni_2SbO_{12}$ because $Li_3Ni_2SbO_{12}$ is isostructural and isoelectronic with $Na_3Ni_2SbO_{12}$, and because $A_3Ni_2SbO_6$ (A = Li, Na) has already been studied [13]. In our DFT + U calculations, we employed the U_{eff} values of 3 and 4 eV, which lead to similar trends (see below).

3.2.2. Spin Exchanges and Zigzag Order

The first, second, and third NN intralayer spin exchanges to consider for $Li_2Ni_2TeO_6$ and $Li_3Ni_2SbO_6$ are presented in Figure 5a, and those for $K_2Ni_2TeO_6$ in Figure 5b. We evaluate these spin exchanges by using the energy-mapping analysis based on DFT calculations [15,20,21]. The three spin exchanges of $K_2Ni_2TeO_6$ (Figure 5b) were determined using the four ordered spin states of Supplementary Figure S3. Similarly, the six intralayer spin exchanges of $Li_2Ni_2TeO_6$ and $Li_3Ni_2SbO_6$ (Figure 5a) were determined using the seven ordered spin states of Supplementary Figures S4 and S5, respectively. In the energy-mapping analysis, we determined the relative energies of the ordered spin states by DFT + U calculations (Supplementary Tables S2–S4), expressed the energies of these states in terms of the spin exchanges (Supplementary Tables S5–S7), and finally mapped the relative energies of the DFT + U calculations to the corresponding relative energies expressed in terms of the spin exchanges to find the values of the spin exchanges.

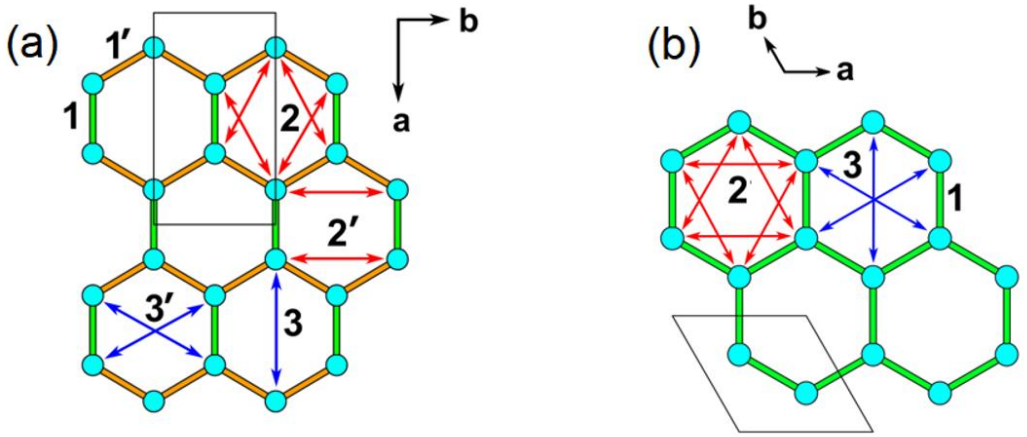

Figure 5. Intralayer spin exchanges defined for $Li_2Ni_2TeO_6$ and $Li_3Ni_2SbO_6$ in (**a**), and for $K_2Ni_2TeO_6$ in (**b**).

The spin exchanges of $A_2Ni_2TeO_6$ (A = K, Li) and $Li_3Ni_2SbO_6$ obtained from the energy-mapping analysis are summarized in Tables 5 and 6, from which we note the following trends: (1) the first NN spin exchanges are all strongly FM, (2) the second NN spin exchanges are all negligible, and (3) the third NN spin exchanges are all strongly AFM. The magnetic order that accommodates these three factors is a zigzag order, as depicted in Figure 1b, which is what has been experimentally observed for $A_2Ni_2TeO_6$ (A = Li, K) and $A_3Ni_2SbO_6$ (A = Li, Na) [13,14]. To understand the occurrence of a short-range magnetic order in these materials, one might consider every FM chain of their zigzag-ordered honeycomb lattices as a pseudo-spin unit. Then, each zigzag-ordered honeycomb lattice is equivalent to an AFM uniform chain, so the short-range order of the zigzag-ordered honeycomb lattice becomes equivalent to that of an AFM uniform chain. Namely, the short-range order in the zigzag-ordered honeycomb lattices of $A_2Ni_2TeO_6$ (A = Li, K) and $A_3Ni_2SbO_6$ (A = Li, Na) is associated with short-range ordering of the FM chains along the direction perpendicular to the chains.

Table 5. Experimental Ni . . . Ni distances (in Å) and calculated spin exchanges (in K), obtained from DFT + U computations, of $Li_2Ni_2TeO_6$ and $Li_3Ni_2SbO_6$.

	$Li_2Ni_2TeO_6$			**$Li_3Ni_2SbO_6$**		
	Ni . . . Ni	**U_{eff} = 3 eV**	**U_{eff} = 4 eV**	**Ni . . . Ni**	**U_{eff} = 3 eV**	**U_{eff} = 4 eV**
J_1	2.961	39.57	31.41	2.983	19.6	16.1
J_1'	2.999	31.39	25.05	2.995	41.7	33.0
J_2	5.178	−1.93	−1.43	5.179	−0.14	−0.08
J_2'	5.160	0.40	0.41	5.183	−2.5	−1.9
J_3	6.019	−33.47	−26.59	5.985	−22.8	−17.7
J_3'	5.949	−40.53	−31.45	5.980	−29.0	−22.8

Table 6. Experimental Ni . . . Ni distances (in Å) and calculated spin exchanges (in K), obtained from DFT + U computations, of $K_2Ni_2TeO_6$.

	Ni . . . Ni	**U_{eff} = 3 eV**	**U_{eff} = 4 eV**
J_1	3.035	26.8	21.2
J_2	5.256	−0.8	−0.6
J_3	6.069	−41.2	−32.2

It is of interest to examine why the zigzag order arises in the honeycomb lattices of $A_2Ni_2TeO_6$ (A = Li, K) and $A_3Ni_2SbO_6$ (A = Li, Na). The magnetic orbitals of the Ni^{2+} ion in a NiO_6 octahedron are the e_g states, namely, the $x^2 - y^2$ and $3z^2 - r^2$ states, which are combined out-of-phase with the 2p orbitals of the surrounding oxygen ligands. Of the two, the $x^2 - y^2$ state can have a substantial interaction in the first and third NN exchange paths, as depicted in Figure 6a,b, respectively, because the NiO_4 square planes containing these orbitals can be coplanar. The first NN exchange consists of two Ni-O-Ni paths, in which the two $x^2 - y^2$ states have their p-orbitals orthogonally arranged at the shared oxygen atoms (Figure 6a). Thus, between the two magnetic orbitals, the overlap integral is zero while the overlap density is nonzero. As a result, the first NN exchange becomes FM [15,20,21,45]. The third NN exchange consists of two Ni-O···O-Ni paths, in which the p-orbital tails of the two $x^2 - y^2$ states are arranged such that the overlap integral is nonzero while the overlap density is practically zero. As a result, the third NN exchange becomes AFM. For the second NN exchange, the NiO_4 square planes containing the $x^2 - y^2$ states cannot be coplanar (see Supplementary Figure S6). Thus, neither the overlap integral nor the overlap density between the two $x^2 - y^2$ states can be substantial, so the second NN exchange is weak.

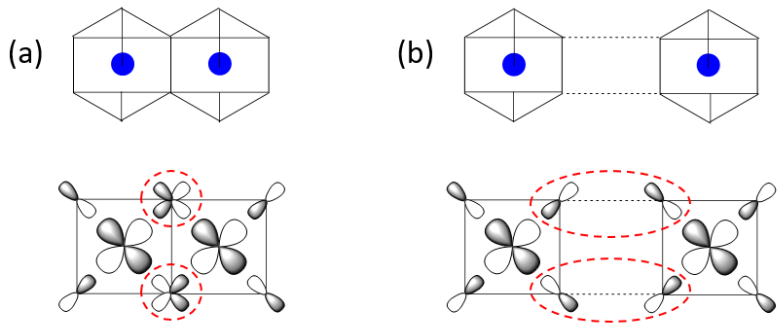

Figure 6. Arrangement of two $x^2 - y^2$ magnetic orbitals (**a**) in the first NN exchange path and (**b**) in the third NN exchange path in a honeycomb lattice of magnetic ions. In (**a**,**b**), the two magnetic orbitals interact through their p-orbital tails in the circled regions. The NiO_6 octahedra are presented to emphasize the square planes containing the $x^2 - y^2$ magnetic orbitals.

Finally, we examined the effective interlayer spin exchanges in $A_2Ni_2TeO_6$ (A = K, Li) and $Li_3Ni_2SbO_6$. What matters in a long-range magnetic ordering in these systems at low temperature is whether the zigzag-ordered honeycomb layers become ferromagnetically or antiferromagnetically ordered (Supplementary Figures S7–S9). Results of these calculations are summarized in Table 7, which predicts that the honeycomb layers should be ferromagnetically coupled. This is in agreement with the experiment for $Li_3Ni_2SbO_6$ [13]. The preference for the FM interlayer coupling is much stronger for $Li_2Ni_2TeO_6$ than for $K_2Ni_2TeO_6$. This reflects that the interlayer distance is shorter for $Li_2Ni_2TeO_6$, which strengthens the interlayer interaction. This result is consistent with the observation that the long-range ordering temperature, T_N, which involves the ordering between the zigzag-ordered honeycomb layers, is greater for $Li_2Ni_2TeO_6$ than for $K_2Ni_2TeO_6$ (~24.4 vs. ~22.8 K).

Table 7. Relative energies (in K per formula unit), calculated from DFT + U computations, of the FM and AFM arrangements between the zigzag-ordered layers in $A_2Ni_2TeO_6$ (A = K, Li) and $Li_3Ni_2SbO_6$.

	$Li_2Ni_2TeO_6$		**$Li_3Ni_2SbO_6$**		**$K_2Ni_2TeO_6$**	
U^{eff}	3 eV	4 eV	3 eV	4 eV	3 eV	4 eV
FM	0	0	0	0	0	0
AFM	6.8	5.3	3.4	2.7	0.6	0.5

4. Concluding Remarks

The static magnetic susceptibility along with specific heat data showed the onset of antiferromagnetic order at $T_N \approx 22.8$ and 24.4 K for $K_2Ni_2TeO_6$ and $Li_2Ni_2TeO_6$, respectively, which is preceded by a short-range order. The high-temperature magnetic susceptibility data exhibited Curie–Weiss behavior, with Weiss temperatures Θ of approximately -13 and -20 K for $K_2Ni_2TeO_6$ and $Li_2Ni_2TeO_6$, respectively. The effective magnetic moment was estimated to be about 4.46 μ_B per formula unit and agrees with the theoretical value expected for Ni^{2+} ($S = 1$) ions. If we were to describe the high-temperature magnetic portion of the susceptibilities of $A_2Ni_2TeO_6$ (A = K, Li), they can be described by a honeycomb with spin exchange $J \approx -8 \pm 1$ K. ESR spectra in the paramagnetic phase showed a single Lorentzian-shaped line, which was attributed to Ni^{2+} ions at octahedral sites, which were characterized by the isotropic effective g-factor 2.20 ± 0.01. In addition, our ESR data indicated an extended region of short-range order correlations, typical of low-dimensional or frustrated magnets. The intralayer spin exchanges evaluated for $A_2Ni_2TeO_6$ (A = K, Li) and $Li_3Ni_2SbO_6$ showed that the honeycomb layers of these magnets adopted a zigzag order, largely because the third nearest-neighbor spin exchanges are strongly antiferromagnetic and because the first nearest-neighbor spin exchanges are strongly ferromagnetic. This finding arises largely from the fact that the spin exchanges between adjacent Ni^{2+} ions are governed largely by their $x^2 - y^2$ magnetic orbitals. Adjacent zigzag-ordered honeycomb layers prefer to be ferromagnetically than antiferromagnetically coupled. The short-range order of the zigzag-ordered honeycomb lattice is equivalent to that of an antiferromagnetic uniform chain, and arises from the short-range ordering of the ferromagnetic chains along the direction perpendicular to the zigzag chains.

Supplementary Materials: The following supporting information can be downloaded at: https://www.mdpi.com/article/10.3390/ma15072563/s1, Section S1 on the crystal structure of $A_2Ni_2TeO_6$, Section S2 on the intralayer spin exchanges, and Section S3 on the intralayer spin exchanges. It includes Figures S1–S10 and Tables S1–S7. References [16,22,46] are cited in the supplementary materials.

Author Contributions: Conceptualization, A.V. and M.-H.W.; methodology, V.N.; formal analysis, J.-S.L. and H.-J.K.; investigation, T.V. and M.E.; writing—original draft preparation, V.N. and M.-H.W.; writing—review and editing, A.V. All authors have read and agreed to the published version of the manuscript.

Funding: This work was supported by the grant 14-03-01122 from the Russian Foundation for Basic Research (VBN), by the Russian Scientific Foundation through Grant No. 22-42-08002, and by the Mega-grant program of the Government of Russian Federation through the project 075-15-2021-604. The work at KHU was financially supported by the Basic Science Research Program through the National Research Foundation (NRF) of Korea, which was funded by the Ministry of Education (2020R1A6A1A03048004).

Data Availability Statement: The original data are available on the request.

Conflicts of Interest: No conflicts of interests are declared.

References

1. Vasiliev, A.; Volkova, O.; Zvereva, E.; Markina, M. Milestones of low-D quantum magnetism. *NPG Quantum Mater.* **2018**, *3*, 18–30. [CrossRef]
2. Kitaev, A. Anyons in an exactly solved model and beyond. *Ann. Phys.* **2006**, *321*, 2–111. [CrossRef]
3. Singh, Y.; Manni, S.; Reuther, J.; Berlijn, T.; Thomale, R.; Ku, W.; Trebst, S.; Gegenwart, P. Relevance of the Heisenberg-Kitaev model for the honeycomb lattice iridates A_2IrO_7. *Phys. Rev. Lett.* **2012**, *108*, 127203. [CrossRef] [PubMed]
4. Stavropoulos, P.P.; Pereira, D.; Kee, H.Y. Microscopic mechanism for a higher-spin Kitaev Model. *Phys. Rev. Lett.* **2019**, *123*, 037203. [CrossRef]
5. Singh, Y.; Gegenwart, P. Antiferromagnetic Mott insulating state in single crystals of the honeycomb lattice material Na_2IrO_3. *Phys. Rev. B* **2010**, *82*, 064412. [CrossRef]

6. Ye, F.; Chi, S.; Cao, H.; Chakoumakos, B.C.; Fernandez-Baca, J.A.; Custelceanu, R.; Qi, T.F.; Korneta, O.B.; Cao, G. Direct evidence of a zigzag spin-chain structure in the honeycomb lattice: A neutron and x-ray diffraction investigation of single-crystal Na_2IrO_3. *Phys. Rev. B* **2012**, *85*, 180403. [CrossRef]
7. Liu, X.; Berlijn, T.; Yin, W.-G.; Ku, W.; Tsvelik, A.; Kim, Y.J.; Gretarsson, H.; Singh, Y.; Gegenwart, P.; Hill, J.P. Long-range magnetic ordering in Na_2IrO_3. *Phys. Rev. B* **2011**, *83*, 220403. [CrossRef]
8. Sandilands, L.J.; Tian, Y.; Plumb, K.W.; Kim, Y.J.; Burch, K.S. Scattering Continuum and Possible Fractionalized Excitations in α-$RuCl_3$. *Phys. Rev. Lett.* **2015**, *114*, 147201. [CrossRef]
9. Sears, J.A.; Songvilay, M.K.; Plumb, W.; Clancy, J.P.; Qiu, Y.; Zhao, Y.; Parshall, D.; Kim, Y.J. Magnetic order in α-$RuCl_3$: A honeycomb-lattice quantum magnet with strong spin-orbit coupling. *Phys. Rev. B* **2015**, *91*, 144420. [CrossRef]
10. Kasahara, Y.; Ohnishi, T.; Mizukami, Y.; Tanaka, O.; Ma, S.; Sugii, K.; Kurita, N.; Tanaka, H.; Nasu, J.; Motome, Y.; et al. Majorana quantization and half-integer thermal quantum Hall effect in a Kitaev spin liquid. *Nature* **2018**, *559*, 227–231. [CrossRef]
11. Takayama, T.; Kato, A.; Dinnebier, R.; Nuss, J.; Kono, H.; Veiga, L.S.I.; Fabbris, G.; Haskel, D.; Takagi, H. Hyperhoneycomb Iridate β-Li_2IrO_3 as a platform for Kitaev magnetism. *Phys. Rev. Lett.* **2015**, *114*, 077202. [CrossRef] [PubMed]
12. Katukuri, V.M.; Yadav, R.; Hozoi, L.; Nishimoto, S.; van den Brink, J. The vicinity of hyper-honeycomb β-Li_2IrO_3 to a three-dimensional Kitaev spin liquid state. *Sci. Rep.* **2016**, *6*, 29585. [CrossRef]
13. Zvereva, E.A.; Stratan, M.I.; Ovchenkov, Y.A.; Nalbandyan, V.B.; Lin, J.-Y.; Vavilova, E.L.; Iakovleva, M.F.; Abdel-Hafiez, M.; Silhanek, A.V.; Chen, X.-J.; et al. Zigzag antiferromagnetic quantum ground state in monoclinic honeycomb lattice antimonates $A_3Ni_2SbO_6$ (A = Li, Na). *Phys. Rev. B* **2015**, *92*, 144401. [CrossRef]
14. Kurbakov, A.I.; Korshunov, A.N.; Podchezertsev, S.Y.; Malyshev, A.L.; Evstigneeva, M.A.; Damay, F.; Park, J.; Koo, C.; Klingeler, R.; Zvereva, E.A.; et al. Zigzag spin structure in layered honeycomb $Li_3Ni_2SbO_6$: A combined diffraction and antiferromagnetic resonance study. *Phys. Rev. B* **2017**, *96*, 024417. [CrossRef]
15. Koo, H.-J.; Kremer, R.; Whangbo, M.-H. Unusual Spin Exchanges Mediated by the Molecular Anion $P_2S_6{}^{4-}$: Theoretical Analyses of the Magnetic Ground States, Magnetic Anisotropy and Spin Exchanges of MPS_3 (M = Mn, Fe, Co, Ni). *Molecules* **2021**, *26*, 1410. [CrossRef]
16. *Powder Diffraction File*; International Centre for Diffraction Data: Newtown Square, PA, USA, 2009; entry 00-059-0445.
17. Grundish, N.S.; Seymour, I.D.; Henkelman, G.; Goodenough, J.B. Electrochemical Properties of Three $Li_2Ni_2TeO_6$ Structural Polymorphs. *Chem. Mater.* **2019**, *31*, 9379–9388. [CrossRef]
18. Masese, T.; Yoshii, K.; Yamaguchi, Y.; Okumura, T.; Huang, Z.-D.; Kato, M.; Kubota, K.; Furutani, J.; Orikasa, Y.; Senoh, H.; et al. Rechargeable potassium-ion batteries with honeycomb-layered tellurates as high voltage cathodes and fast potassium-ion conductors. *Nat. Comm.* **2018**, *9*, 3823–3835. [CrossRef]
19. Matsubara, N.; Nocerino, E.; Forslund, O.K.; Zubayer, A.; Papadopoulos, K.; Andreica, D.; Sugiyama, J.; Palm, R.; Guguchia, Z.; Cottrell, S.P.; et al. Magnetism and ion diffusion in honeycomb layered oxide $K_2Ni_2TeO_6$. *Sci. Rep.* **2020**, *10*, 18305–18318. [CrossRef]
20. Xiang, H.J.; Lee, C.; Koo, H.-J.; Gong, X.; Whangbo, M.-H. Magnetic properties and energy-mapping analysis. *Dalton Trans.* **2013**, *42*, 823–853. [CrossRef]
21. Whangbo, M.-H.; Xiang, H.J. Magnetic Properties from the Perspectives of Electronic Hamiltonian: Spin Exchange Parameters, Spin Orientation and Spin-Half Misconception. In *Handbook in Solid State Chemistry, Volume 5: Theoretical Descriptions*; Wiley: Hoboken, NJ, USA, 2017; pp. 285–343.
22. Evstigneeva, M.A.; Nalbandyan, V.B.; Petrenko, A.A.; Medvedev, B.S.; Kataev, A.A. A New Family of Fast Sodium Ion Conductors: $Na_2M_2TeO_6$ (M = Ni, Co, Zn, Mg). *Chem. Mater.* **2011**, *23*, 1174–1181. [CrossRef]
23. Paulsen, J.M.; Donaberger, R.A.; Dahn, J.R. Layered T2-, O6-, O2-, and P2-Type $A_{2/3}[M'^{2+}{}_{1/3}M^{4+}{}_{2/3}]O_2$ Bronzes, A = Li, Na; M′ = Ni, Mg; M = Mn, Ti. *Chem. Mater.* **2000**, *12*, 2257–2267. [CrossRef]
24. Shannon, R. Revised effective ionic radii and systematic studies of interatomic distances in halides and chalcogenides. *Acta Cryst.* **1976**, *A32*, 751–767. [CrossRef]
25. Gagné, O.; Hawthorne, F. Comprehensive derivation of bond-valence parameters for ion pairs involving oxygen. *Acta Cryst.* **2015**, *B71*, 562–578. [CrossRef] [PubMed]
26. Bain, G.A.; Berry, J.F. Diamagnetic Corrections and Pascal's Constants. *J. Chem. Educ.* **2008**, *85*, 532–536. [CrossRef]
27. Rushbrook, G.S.; Wood, P.J. On the Curie points and high temperature susceptibilities of Heisenberg model ferromagnetics. *Mol. Phys.* **1958**, *1*, 257–283. [CrossRef]
28. Abragam, A.; Bleaney, B. *Electron Paramagnetic Resonance of Transition Ions*; Clarendon Press: Oxford, UK, 1970; 700p.
29. Joshi, J.P.; Bhat, S.V. On the analysis of broad Dysonian electron paramagnetic resonance spectra. *J. Magn. Reson.* **2004**, *168*, 284–287. [CrossRef]
30. Kawasaki, K. Anomalous Spin Relaxation near the Magnetic Transition. *Prog. Theor. Phys.* **1968**, *39*, 285–311. [CrossRef]
31. Kawasaki, K. Ultrasonic attenuation and ESR linewidth near magnetic critical points. *Phys. Lett. A* **1968**, *26A*, 543. [CrossRef]
32. Mori, H.; Kawasaki, K. Antiferromagnetic Resonance Absorbtion. *Prog. Theor. Phys.* **1962**, *28*, 971–987. [CrossRef]
33. Huber, D.L. Critical-Point Anomalies in the Electron-Paramagnetic-Resonance Linewidth and in the Zero-Field Relaxation Time of Antiferromagnets. *Phys. Rev. B* **1972**, *6*, 3180–3186. [CrossRef]
34. Richards, P.M. Critical exponents for NMR and ESR linewidths in a two-dimensional antiferromagnet. *Solid State Commun.* **1973**, *13*, 253–256. [CrossRef]

35. Anders, A.G.; Volotski, S.V. EPR in 1-d and 2-d antiferromagnetic systems. *J. Magn. Magn. Mater.* **1983**, *31–34*, 1169–1170. [CrossRef]
36. Zvereva, E.A.; Savelieva, O.A.; Titov, Y.D.; Evstigneeva, M.A.; Nalbandyan, V.B.; Kao, C.N.; Lin, J.-Y.; Presniakov, I.A.; Sobolev, A.V.; Ibragimov, S.A.; et al. A new layered triangular antiferromagnet Li_4FeSbO_6: Spin order, field-induced transitions and anomalous critical behavior. *Dalton Trans.* **2013**, *42*, 1550–1566. [CrossRef] [PubMed]
37. Fisher, M.E. Lattice statistics in a magnetic field, I. A two-dimensional super-exchange antiferromagnet. *Proc. R. Soc. Lond. Ser. A* **1960**, *254*, 66–85.
38. Fisher, M.E. Relation between the specific heat and susceptibility of an antiferromagnet. *Philos. Mag.* **1962**, *7*, 1731–1743. [CrossRef]
39. Losee, D.B.; McElearney, J.N.; Shankle, G.E.; Carlin, R.L.; Cresswell, P.J.; Robinson, W.T. An anisotropic low-dimensiomal Izing system, $[(CH_3)_3NH]CoCl_32H_2O$: Its structure and canted antiferromagnetic behavior. *Phys. Rev. B* **1973**, *8*, 2185–2199. [CrossRef]
40. Blöchl, P.E. Projector augmented-wave method. *Phys. Rev. B* **1994**, *50*, 17953–17979. [CrossRef]
41. Kresse, G.; Joubert, D. From ultrasoft pseudopotentials to the projector augmented-wave method. *Phys. Rev. B* **1999**, *59*, 1758–1775. [CrossRef]
42. Kresse, G.; Furthmüller, J. Efficient iterative schemes for ab initio total-energy calculations using a plane-wave basis set. *Phys. Rev. B* **1996**, *54*, 11169–11186. [CrossRef]
43. Perdew, J.P.; Burke, K.; Ernzerhof, M. Generalized gradient approximation made simple. *Phys. Rev. Lett.* **1996**, *77*, 3865–3868. [CrossRef]
44. Dudarev, S.L.; Botton, G.A.; Savrasov, S.Y.; Humphreys, C.J.; Sutton, A.P. Electron-energy-loss spectra and the structural stability of nickel oxide: An LSDA+U study. *Phys. Rev. B* **1998**, *57*, 1505. [CrossRef]
45. Whangbo, M.-H.; Koo, H.-J.; Kremer, R.K. Spin Exchanges between Transition Metal Ions Governed by the Ligand p-Orbitals in Their Magnetic Orbitals. *Molecules* **2021**, *26*, 531. [CrossRef] [PubMed]
46. Sudorgin, N.G.; Nalbandyan, V.B. Quantitative X-ray monitoring of electrode processes in sealed cells. Reduction of zirconium β-molybdate by lithium. *Soviet Electrochem.* **1992**, *28*, 100–102.